npj | Quantum Materials

www.nature.com/npjquantmats

ARTICLE OPEN

Measurement of the atomic orbital composition of the near-fermi-level electronic states in the lanthanum monopnictides LaBi, LaSb, and LaAs

Thomas J. Nummy[1,2], Justin A. Waugh[1,2], Stephen P. Parham[1,2], Qihang Liu[3], Hung-Yu Yang[4], Haoxiang Li[1,2], Xiaoqing Zhou[1,2], Nicholas C. Plumb[5], Fazel F. Tafti[4] and Daniel S. Dessau[1,2,6]

Recent debates in the literature over the relationship between topology and Extreme Magnetoresistance (XMR) have drawn attention to the Lanthanum Monopnictide family of binary compounds. Angle resolved photoemission spectroscopy (ARPES) is used to measure the electronic structure of the XMR topological semimetal candidates LaBi, LaSb, and LaAs. The orbital content of the near-E_F states in LaBi and LaSb are extracted using varying photon polarizations and both dominant *d* and *p* bands are observed near *X*. The measured bulk bands are shifted in energy when compared to the results of Density Functional Calculations. This disagreement is minor in LaBi, but large in LaSb and LaAs. The measured bulk band structure of LaBi shows a clear band inversion and puts LaBi in the $\upsilon = 1$ class of Topological Insulators (or semimetals), as predicted by calculations and consistent with the measured Dirac-like surface states. LaSb is on the verge of a band inversion with a less-clear case for any distinctly topological surface states and in disagreement with calculations. Lastly, these same bands in LaAs are clearly non-inverted implying its topological triviality and demonstrating a topological phase transition in the Lanthanum monopnictides. Using a wide range of photon energies the true bulk states are cleanly disentangled from the various types of surface states which are present. These surface states exist due to surface projections of bulk states in LaSb and for topological reasons in LaBi.

npj Quantum Materials (2018)3:24 ; doi:10.1038/s41535-018-0094-3

INTRODUCTION

The binary compounds containing a single pnictogen element with La in a rock salt crystal structure have recently drawn attention in the literature for both demonstrating extreme magnetoresistance (XMR) as well as possible topological states and surface Dirac Fermions.[1–6] Here magnetoresistance is defined by the ratio $R(H)/R(0)$, where *R* is the electrical resistance and *H* is the applied magnetic field. In transition metal oxides, both Giant and Colossal Magnetoresistance have been observed[7,8] and implemented in non-volatile magnetic memory,[9] as magnetic sensors,[10] as well as proposed spin valves in spintronics.[11] XMR is distinct from these well-understood phenomena in that it is exhibited in materials where $R(0)$ is small, i.e., good metals.[12] The effect also spans several classes of materials including Dirac semimetals,[13,14] Weyl semimetals,[15–17] and layered semimetals.[18–20]

The complete physical description of the mechanism responsible for XMR is currently not understood. Quantum oscillation studies in the partially electron-hole compensated LaSb and LaBi have shown that the electrical transport at low temperature and applied magnetic field is dominated by ellipsoidal electron pockets.[12] Due to the spin-orbit coupling in both of these materials, electronic structure calculations predict mixing between the La *d* orbital and the pnictogen *p* orbital bands, which compose the pocket.[2,12] The mixing of these two bands, in turn, creates an orbital composition crossover at E_F on this pocket. The existence of this crossover is found in many of the materials which exhibit XMR.[12] Furthermore, topological surface states have been suggested as a necessary ingredient for XMR.[21,22] Several of the materials which demonstrate XMR have been confirmed or predicted to be, topologically non-trivial[15–17,21] indicating, at minimum, a correlation between the two phenomena.

Electronic structure calculations on the Lanthanum Monopnictides indicate that the *d* and *p* bands will cross only once along the $\Gamma - X$ direction and therefore will be inverted at *X*.[2] This inversion, along with the existence of inversion and time reversal symmetries in these systems, would result in a non-trivial Z_2 invariant for the Lanthanum Monopnictides. The same calculations show the degree of band inversion in a given Lanthanum Monopnictide compound is dependent on the pnictogen species present. Furthermore, these results predict that the inversion magnitude decreases with a smaller atomic number, but is present in all compounds in the family except LaN.[2]

In this report, we present ARPES measurements as well as bulk electronic structure calculations for LaSb, LaBi, and LaAs. Three-dimensional mapping of *k* space is performed and shows good but not complete agreement with the Density Functional electronic structure calculations, with the most important differences concerning the inversion of the bands at the X point,

[1]Department of Physics, University of Colorado, Boulder, CO 80309, USA; [2]JILA, National Institute of Standards and Technology, and Department of Physics, University of Colorado, Boulder, CO 80309, USA; [3]Renewable and Sustainable Energy Institute, University of Colorado, Boulder, CO, USA; [4]Department of Physics, Boston College, Boston, MA 02467, USA; [5]Swiss Light Source, Paul Scherrer Institut, CH-5232 Villigen, Switzerland and [6]Center for Experiments on Quantum Materials, University of Colorado, 2000 Colorado Ave, Boulder, CO 80309, USA
Correspondence: Thomas J. Nummy (thomas.nummy@colorado.edu)

Received: 21 April 2017 Revised: 7 March 2018 Accepted: 19 March 2018
Published online: 25 May 2018

which impacts the topological order of the materials. A full mapping of k_z using ARPES over several Brillouin zones (BZ) shows the presence of several surface effects in the spectra from both LaBi and LaSb, including unique surface states in LaBi. We make a comparative study of the surface states in both materials with a discussion on the topological nature of these surface states. Furthermore, we utilize the selection rules of the photoemission matrix element to directly extract the orbital composition of the electron pockets found in the bulk of these materials. We report a clear band inversion in LaBi, while LaSb is near a band inversion, and LaAs is clearly non-inverted.

Previous ARPES studies have been carried out on LaBi and LaSb focusing on their surface states and corresponding topological classification: in LaBi,[6,21,22] and in LaSb.[2,21] However, the topological class of these materials is inferred from calculations and the existence of "Dirac-like" dispersions in each of these reports. The consensus reached by refs.[6,21,22] is that LaBi is topologically nontrivial. Ref. [4] claims LaSb to be topologically trivial while ref. [21] argues that LaSb is non-trivial.

From direct measurement, we show that LaBi has a band inversion, LaSb is on the verge of inversion, and LaAs is non-inverted. This demonstrates a topological phase transition within the family of Lanthanum Monopnictides. As for implications to XMR, we note that only LaBi is topologically non-trivial. From these facts, we conclude the possibility that topology is an essential ingredient for XMR is unlikely.

RESULTS

Single crystals of LaBi, LaSb, and LaAs were cleaved in-situ along a 100 crystal face. The presence of a surface termination allows for the possibility of surface states which follow the symmetries of the surface Brillouin zone (SBZ), which are distinct from the bulk Brillouin zone. The relationship between the two zones is shown in black (bulk) and blue (surface) in Fig. 1c. Note that when cleaved on the 100 surface, Γ and one of the three bulk X points, X_3, is located at $k_{||} = 0$. Therefore, when projected along the $k_\perp$ (k_z) direction, they overlap at the same high symmetry point in the SBZ: $\bar{\Gamma}$. Similarly, the bulk X_2 and W points both project to the surface $\bar{M}$ point. These projections to the SBZ require an in-plane back folding of states in the SBZ relative to bulk states, as will be discussed in more detail later in the paper. These surface states or surface resonances need to be distinguished from topologically induced surface states.

Results of Density Functional calculations for LaBi and LaSb materials are presented in Fig. 1a, showing the bulk Fermi surface to have two hole pockets centered on the Γ point and ellipsoidal electron pockets centered on the X points. These electron pockets have been indicated to dominate the transport signal in quantum oscillation experiments at low temperature and high magnetic field, the same regime of phase space as XMR.[12]

The experimental Fermi surfaces as captured by our ARPES measurements are very similar to the calculations, as shown in Fig. 1b,d. Starting from the stacked three-dimensional bulk Brillouin zones shown in Fig. 1e, we may take in-plane experimental cuts (panel B), or we may hold an in-plane value such as k_y fixed, and take a "vertical" slice in k_z such as is shown in panel D. The vertical slices in which k_z is varied allow us to accurately select the high symmetry in-plane cuts (for example, the cuts of panel B were taken at $k_z = 6^*(2\pi/a)$, equivalent to $k_z = 0$). Furthermore, these cuts allow us to distinguish between true bulk states, which disperse in k_z and states localized near the surface, which do not. More details of this will be discussed in a later section, including in the Supplementary Materials, which shows the conversion from photon energies to k_z values.

Visible in panel 1B are the "jack-shaped" hole pockets on the Fermi surface, centered at the Γ points $((kx, ky, kz) = (0, 0, 6), (0, 2, 6), (2, 0, 6), (2, 2, 6)$ in units of $2\pi/a$), as well as the many in-plane ellipsoidal electron pockets on the Fermi surface at the bulk X_1 and X_2 points $((kx, ky, kz) = (0, 1, 6), (1, 0, 6), (1, 2, 6)$, etc). These are exactly as expected from the bulk calculations. The out-of-plane ellipsoids are visible at the X_3 point, i.e.,: $(kx, ky, kz) = (1, 1, 6), (1, -1, 6)$, etc. These in-plane momenta correspond to $\bar{\Gamma}$ in the SBZ, as do (1,1,6) and $(1, -1,6)$ and a superposition of spectral weight can be seen around the circular cross-section of the ellipsoid at X_3 from $\bar{\Gamma}$, resulting in a faint jack-shape. This weight in panel 1B

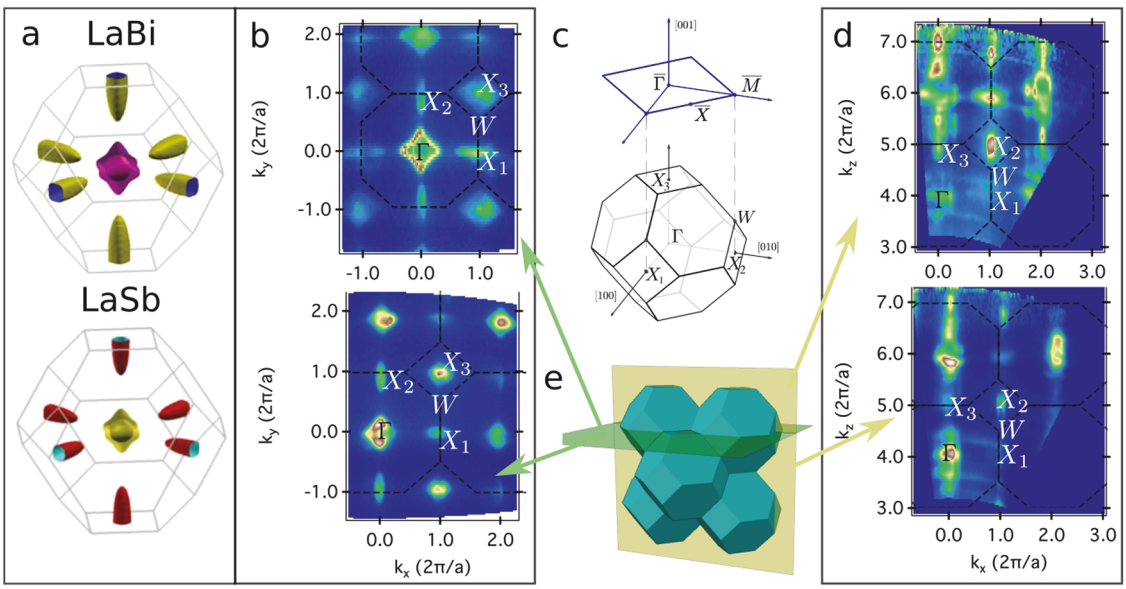

Fig. 1 Determination of the Fermi surface by k space mapping. **a** Calculated Fermi surface for LaBi (top) and LaSb (bottom). Both compounds have ellipsoidal electron pockets centered on the X points and two hole pockets centered on the Gamma point. **b** Fermi surfaces measured in the k_x, k_y plane at $k_z = 6.0$ (π/a). **c** Schematic of the Brillouin Zone projected to the surface Brillouin Zone. **d** Measured Fermi surfaces from ARPES in the k_x, k_z plane covering two Brillioun zones in the k_z direction with k_y fixed at 0. **e** Planes of fixed $k_y = 0$ (yellow) and $k_z = 6$ (π/a) (green) illustrate the location of the constant energy surfaces in **b**, **c**, which cut through the tessellated truncated octahedra

should be considered as originating from the surface which backfolds spectral weight to the smaller SBZ and/or projects weight to surface states and surface resonances, as will be discussed later.

Understanding the orbital character of the bands is a powerful method to determine the topological classification of a material with inversion and time reversal symmetries.[23,24] Projecting our Density Functional calculations to an atomic orbital basis, we see that for both LaBi and LaSb, the X-point ellipsoidal bands near the Fermi energy are composed of both La *d* orbitals and pnictogen *p* orbitals, as shown in Fig. 2e. The tips of the ellipsoidal electron pockets are majority composed of *d* orbitals, while the midsections of the ellipsoids are of a dominant *p* orbital character. This is consistent with other calculations on the Lanthanum Monopnictides.[2,12]

We employ polarization dependent ARPES to confirm the orbital character determined by DFT. Applying symmetry arguments to the photoemission matrix element[25,26] in conjunction with dipole selection rules, allows us to extract the parity and atomic orbital composition of the electronic wavefunction. This is achieved by comparing the photoemission intensity when the perturbing electric field is even versus odd in the plane defined by the Poynting vector of the light and the sample normal.

Figures 2b, c show the ARPES results for different polarizations and experimental geometries, focusing on the ellipsoidal pockets at the X points. To change the relative orientation of the electron pockets to the Poynting vector of the light, we change the photon energy to move between different k_z planes, namely the X_2 point at $k_z = 5(2\pi/a)$ (2B and 2C, left panel) and the X_1 point at $k_z = 6(2\pi/a)$ (2B and 2C, right panel). This allows us to minimize tilting away from the high symmetry plane of the crystals, keeping the symmetry analysis as pure as possible.

For σ polarized light (Fig. 2b), the central regions of the ellipses are not visible, for either orientation. Via the dipole selection rules, these results imply a lack of in-plane *p* orbitals along the midsection of the ellipse (see Supplementary Materials for more details). The tips of the ellipses give non zero intensity at X_1, and very faint intensity at X_2. We attribute this faint intensity at X_2 to be from impure σ polarization due to the nearly 10° tilting of the sample relative to the Poynting vector at this k_y value. These results for the tips of the ellipsoids require a *d* orbital odd under reflection in the k_z/k_x plane. To determine the specific *d* orbital we note that crystal symmetry requires each ellipsoidal tip to transform into each other under rotations. The only *d* orbital consistent with this constraint for an ellipsoidal pocket pointing in the x-direction is d_{yz} (Fig. 2d).

When using π polarized light (Fig. 2c), a higher intensity signal from the central region of the ellipse is measured, regardless of the relative in-plane orientation of the ellipse to the polarization vector (i.e., both left and right plots of panel C). Using dipole selection rules we conclude the *p* orbitals along the midsection of the ellipse must be out of plane (see Supplementary Materials). This is consistent with our previous conclusion from the σ polarization measurement. Using π polarization at X_1, again we see that the zero in intensity at the tip of the ellipse implies that the *d* orbital there must be odd under reflection in the k_z,k_x plane which is consistent with the d_{yz} orbital.

From these two measurements, subsequent symmetry arguments, and our simulation we can extract the full orbital content of the electron pockets at the *X* points. For the ellipsoids pointing along the x-direction, the tips of the ellipsoids are composed of La d_{yz} orbitals while the equators are composed of tangential pnictogen *p* orbitals as shown in Fig. 2d. A more detailed description of this analysis is given in the Supplementary Materials.

Figure 3 shows a detailed view of the measured dispersions along the high symmetry directions for both materials along with the surface (blue) and bulk (black) Brillouin zones. Panels A (B) and C (D) shows the raw data from the $\Gamma - X$ and $X - W$ cuts respectively for LaBi (LaSb). The second derivative of the data (panels E and F) is used to highlight the dispersive features of the raw data and is shown overlaid with a trace of the dispersions. Blue dashed lines indicate a dominant *p* orbital character of the band as determined from the polarization-dependent ARPES

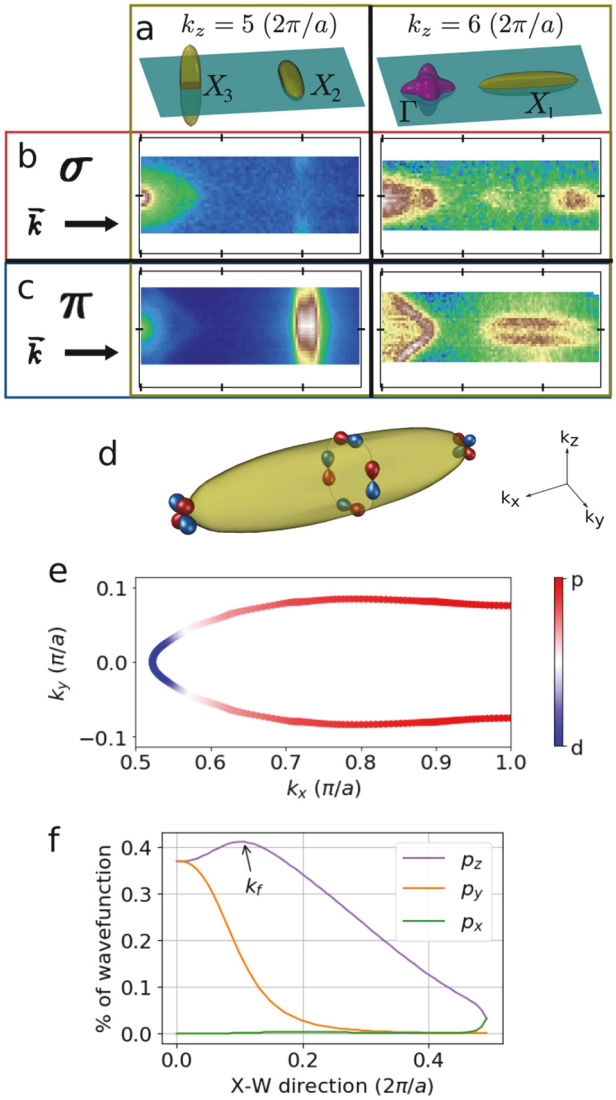

Fig. 2 Determination of atomic orbitals by linear dichroism. **a** Schematic of the 3D Fermi surface relative to the constant energy in-plane momentum cuts shown below in the polarization dependent ARPES results from the electron pockets at *X*. The measurement plane through X_3 and X_2 on the zone edge ($k_z = 5\ (2\pi/a)$) is shown in the left panel. The measurement plane through Γ and X_1 ($k_z = 6\ (2\pi/a)$) is shown in the right panel. **b** ARPES measurements of the Fermi surface using π polarized light incident from the left and (**c**) (σ) polarized light incident from the left. π polarization produces a strong signal from the center of the ellipse, while σ polarization gives a stronger signal from the ends. We conclude that dominant orbital composition of the ellipsoid pocket is that of the schematic shown in **d**. Tangentially ordered *p* orbitals compose the central region of the prolate ellipsoid with d_{yz} orbitals composing the ends. **e** Total *p* vs. total *d* orbital contribution to the electron pocket shown at E_F. **f** Relative contributions from different *p* orbitals to the highest energy occupied band along the X-W direction. k_F is indicated in the diagram to show where the ARPES measurements were performed. The p_z orbital is the dominant contributor to the wavefunction at E_F along this *k* direction

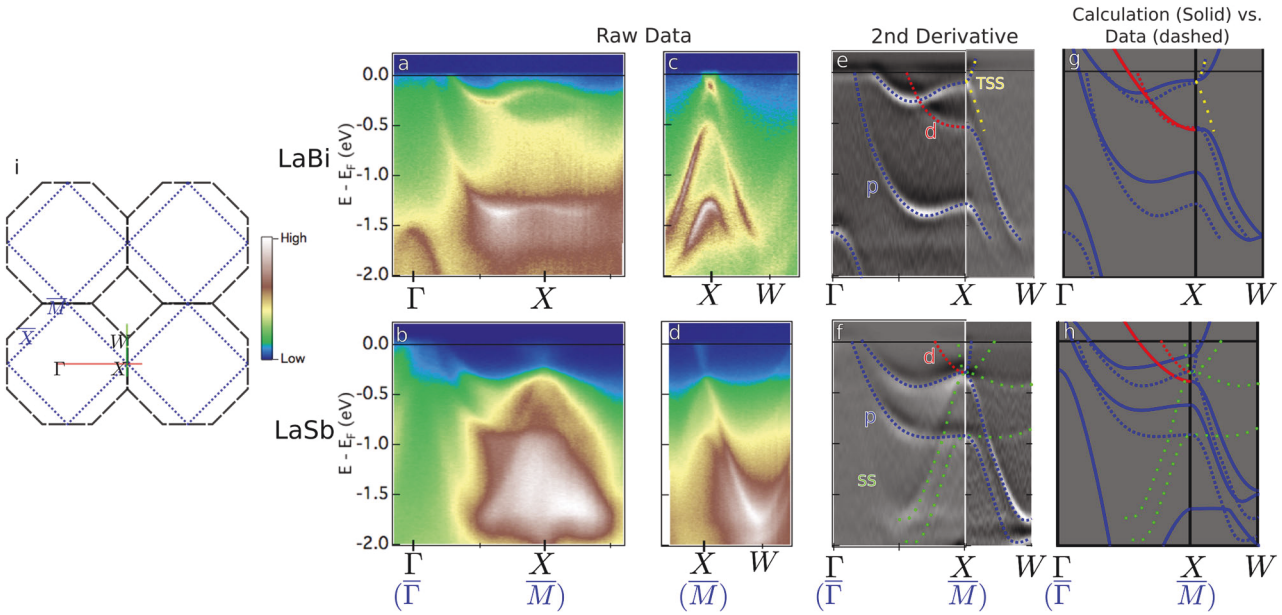

Fig. 3 ARPES dispersions. ARPES dispersions along the $\Gamma - X$ direction for LaBi (**a**) and LaSb (**b**) as well as the *X*-*W* direction for LaBi (**c**) and LaSb (**d**). **e**, **f**: 2nd derivatives of the ARPES data along Γ-*X*-*W* for LaBi and LaSb respectively. The dotted lines are traces of the band dispersions. Blue (Red) denotes P (**d**) orbital dominated bands. Green dashed lines denote bands which arise due to the presence of the crystal surface (SS). Yellow dashed lines indicate a topological surface state (TSS). In LaBi, projecting the bulk density of states to the 001 surface produces a gap at $\overline{M}$ in which the surface state resides, ie. a true surface state. In LaSb, there is no gap at $\overline{M}$ when projecting to the 001 surface. Instead, the bands marked by green are back folded along the k_z direction by π/a by the surface. **g**, **h**: Comparisons between calculated band dispersions (solid lines) and measured band dispersions (dashed lines). In LaBi (**g**) the band inversion at *X* is predicted correctly. In LaSb (**h**), the calculation predicts a band inversion at *X*, however, the experimental results suggest LaSb is at, or very near, a critical point of band inversion. **i** In-plane projection of the bulk BZ (black dashed line) and surface BZ (blue dashed line). The solid red (green) line indicates the location of the cuts in **a**–**d**

experiments of Fig. 2, as well as from orbital-projections of our DFT calculations. Red dashes indicate a dominant *d* orbital character, green and yellow dashes indicate different electronic states that arise due to the presence of the crystal surface and will be described in more detail later.

Panels G and H compile the measured band dispersions (dashed lines, reproduced from panels E and F) with calculated dispersions from DFT (solid red and blue lines). The calculated bands we show are nearly identical to the results from other works,[2,12] and while they have many close similarities to our experimental bulk bands, they also have some clear differences. In particular, we see that many of the calculated *p*-bands from both LaBi and LaSb are shallower in energy and have less dispersion than the experiment, and the calculated *d* bands are deeper in energy than the experiment. Most important are the energies of the states at the *X* point, as these determine whether these materials lie in the $\nu = 1$ topological class or not. As shown in Fig. 3g, the actual agreement between experiment and theory for the LaBi bands at the *X* point is very good, with the *d* band, at 0.55 eV, underneath the *p* band, at 0.1 eV, (inverted) by about 450 meV. This 450 meV inversion gap will be seen to host topological Dirac-like states at the surface (yellow dashed), which are presumably directly related to this band inversion.

In LaSb, the disagreements between the calculations and the experiments become much more important, as shown in panel H. The bulk bands from the Density Functional calculation (solid) show the *d* band at 0.5 eV at *X* to be about 300 meV below the *p* band at 0.2 eV at *X* (inverted), the experimental result of this inversion (dashed lines) is approximately 0 ± 50 meV, i.e., it is not clear whether the bulk bands are inverted or not, therefore we describe LaSb as being on the verge of a topological transition. This will be discussed in more detail in Fig. 4 below.

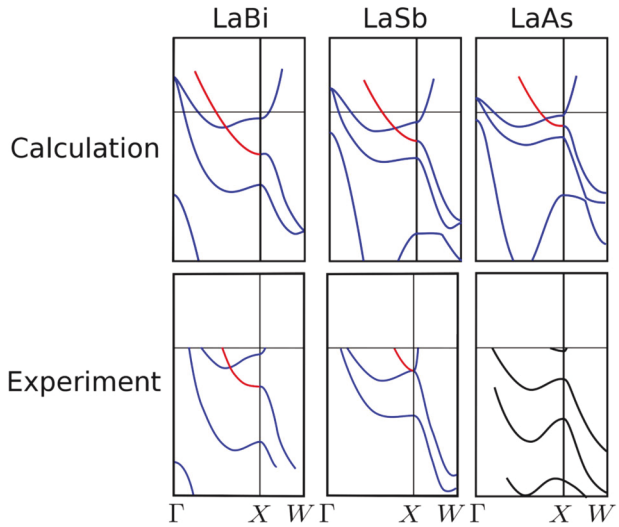

Fig. 4 Top Row: Band structure calculations of LaBi (left), LaSb (center), and LaAs (right). Red (Blue) lines indicate bands with a dominant *d* (*p*) orbital components. A band inversion is predicted in all three materials and therefore all are predicted to be topologically non-trivial. Bottom Row: Measured band structure of LaBi (left), LaSb (center), and LaAs (right). LaBi is still clearly inverted at X, while LaSb lies very near the critical point of topological triviality. The right panel shows that the un-inverted band structure in LaAs. This demonstrates a topological transition within the chemical family

DISCUSSION

Due to the band inversions that are present at the 3 *X* points, LaBi can be classified as a 3D topological semi-metal and should host Dirac-like surface states. However, different surface effects can

manifest similarly in ARPES. Therefore, it is important to confirm topologically driven origins. We start with a discussion which shows that the type of surface states in LaSb are different from those in LaBi. Later, we discuss the results of LaAs and show it is topologically trivial. This progression between the two classes of $\mathbb{Z}_2$ topology demonstrates a topological phase transition in the Lanthanum monopnictides.

Figure 3c shows clear evidence of a Dirac-like dispersion in LaBi centered at the X point ($\overline{M}$ point in the SBZ), which is not present in the bulk Density Functional calculations. To prove that this state is, in fact, a topological surface state (TSS) one must demonstrate the correct number of band inversions exist in the bulk band structure in addition to confirming the state in question is localized to the surface. Projecting the bulk density of states of LaBi along the $W-X$ direction to $\overline{M}$ in the [001] SBZ, one can see that there will be a 450 meV direct gap in which only a pure surface state can reside. These states exist within the bulk band gap and also do not disperse in k_z (See Supplemental Information) from the top of the cone down to the valence band. Therefore this state must be localized to the surface.

This information, together with the existence of the band inversion, produces the conclusion that this is a TSS, consistent with previous reports.[21,22] We label these by the yellow dashed lines in Fig. 3e. The bulk conduction band near X (shown with blue dashed lines) is still present in the ARPES data but is overlapped with the TSS at this location in Fig. 3e,g. The superposition of bulk and surface states is confirmed by considering the k_z behavior. In Fig. 1 panel D we show the Fermi surface in the k_z/k_x plane. There is clear periodicity at the X points, indicating bulk states (for a view of the dispersion along the $X-W-X$ direction in k_z see the Supplementary Fig. S2c,d). The existence of the superimposed TSS is made clear in Supplementary Fig. S3 which shows a Dirac cone that is non-dispersive in k_z and overlaps with the bulk X point. Note that because the X_3 point will project to the $\overline{\Gamma}$ surface point of the [001] surface, one also should expect a very low-intensity topological surface state there at the same energy, though the matrix element for observing this state is strongly suppressed in our data, which emphasize the states at X_1.

In LaSb the states observed in ARPES that are not present in DFT calculations are of a separate nature. The same band inversion found in LaBi along the $\Gamma-X$ direction is predicted to exist in our own DFT calculations (Shown in Fig. 4). However, there are conflicting DFT[2,27] and ARPES[2,21] studies in the literature that claim the existence of, or lack thereof, a TSS in LaSb. Experimental results (Fig. 3f) show that LaSb is very near the critical point of a band inversion at X, however, we observe no obvious TSS. Although Figs. 3b, d appear to show Dirac-like states at X, we find that these are instead replica bands of the bulk dispersion back-folded due to the presence of the crystal surface (which has a smaller, and therefore back-folded Brillouin zone compared to the bulk), which are shown as green dashed lines in Fig. 3f. These back-folded states explain all of the "extra" observed spectral features not predicted by bulk DFT calculations (see Supplementary Materials for a more detailed discussion of this back-folding and k_z resolution). The assignment of all bands in LaSb to either bulk or surface-back-folded bands means there is no evidence of a separate Dirac-like topological surface state (TSS) observed in LaSb, in contrast to the case of LaBi which does have the additional TSS.

Compared to LaBi and LaSb, LaAs is the lightest compound of the three materials. Figure 5 shows the ARPES results from LaAs. Panels (B) and (C) show the $\Gamma-X$ and $X-W$ cuts respectively. The bands of LaAs are clearly non-inverted and therefore LaAs belongs to the topologically trivial ($\nu=0$) class of materials. In Fig. 4, we compile the evidence for the existence of a topological transition in the Lanthanum Monopnictides. The top row shows our density functional calculations for (from left to right) LaBi, LaSb, and LaAs along the $\Gamma-X$ direction. The calculations show a trend of

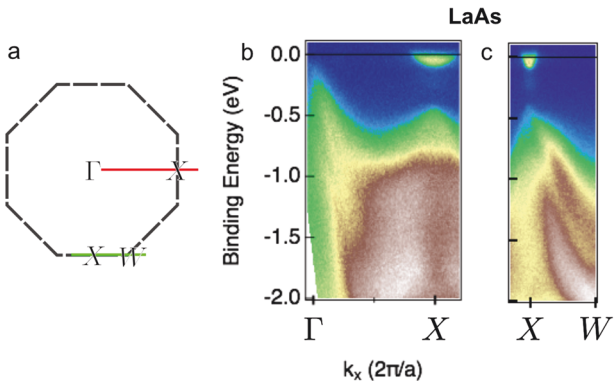

Fig. 5 ARPES dispersions in LaAs. **a** Location of the ARPES cuts in panels **b** (red) and **c** (green). **b** $\Gamma-X$ cut showing the ellipsoidal electron pocket and non-inverted band structure at X. **c** $X-W$ cut across the minor axis of the ellipsoid

decreasing magnitude of the La d band inversion over the pnictogen p band as both the lattice constant and spin-orbit coupling decrease in the lighter pnictogen species, though the inversion is still present in LaAs in these calculations and others.[2] However, our measurements (bottom row) show that in moving from LaBi (left) to LaAs (right) in the pnictogen family the bands are already non-inverted.

An important consequence of the LaAs measurements is that the bands can be non-inverted and still preserve the mass anisotropy and orbital texture of the ellipsoidal electron pockets at X. If the occurrence of XMR in the LaBi and LaSb were due to the topological non-triviality of these compounds and not the orbital crossover on the electron pockets, then LaAs is an ideal test case for determining the role of topology in the mechanism for XMR in the Lanthanum Monopnictides. At this time we are unaware of any studies of ARPES or XMR in the lighter siblings LaP, or LaN.

We have presented ARPES measurements in which we successfully extract the dispersions in LaBi, LaSb, and LaAs. In addition to this, we determine the dominant orbital contributions of the bands in LaBi and LaSb. From our extraction of the orbital character of the near Fermi surface bands and the ARPES dispersions, we show that LaBi has a clear band inversion at X while LaSb appears to be very near a critical point between trivial and nontrivial topological phases, but does not host an obvious TSS. LaAs clearly lies on the other side of this phase transition in the class of trivial topology. For LaSb and LaAs, this differs from both our own DFT calculations and those in the literature. We observe a topological phase transition in the Lanthanum monopnictides which, argues against a clean role of the topology to the XMR effect.

METHODS

The ARPES measurements were done at the Surface/Interface Spectroscopy (SIS) beam line at the Swiss Light Source and the 'I-05' beamline at Diamond Light Source. For both beam lines, a VG-Scienta R4000 electron analyzer was used. The photon energies used were from 20 to 240 eV with a total experimental resolution between ~20 and ~150 meV over this range. The angular resolution of the electron lens is 0.2°, corresponding to 0.01 $Å^{-1}$ at 120 eV electron kinetic energy. Both beam lines utilize undulators with polarization control. Preparation of the crystals for the ARPES measurement was done in a nitrogen-purged glove box. A pristine sample surface was obtained by cleaving the crystals in situ in a working vacuum better than 5×10^{-11} mbar. Proper alignment of the electron analyzer slit to the crystal axes was achieved to a 0.2 degree precision using 6 axis manipulators by performing maps of the electronic dispersion near E_F.

Density functional theory (DFT) with the projector-augmented wave pseudopotential and the generalized gradient approximation to exchange

and correlation of Perdew, Burke and Ernzerhof as implemented in the Vienna ab initio package (VASP) was utilized. The plane wave basis set size reflected in energy cutoff is 500 eV, and the total energy minimization was performed with a tolerance of 10^{-5} eV. Spin-orbit coupling is calculated self-consistently by a perturbation, $\sum_{i,l,m} V_l^{SO} \vec{L} \cdot \vec{S} |l,m,i\rangle\langle l,m,i|$ to the pseudopotential, where $|l,m,i\rangle$ is the angular momentum eigenstate of i-th atomic site. The orbital intensity was calculated by projecting the wave functions, $\psi\left(\vec{k}\right)$, with a plane-wave expansion on the orbital basis (spherical harmonics) of each atomic site, as written in the following:

$$I_n^{(i,l,m)}\left(\vec{k}\right) = \left\langle \psi\left(\vec{k}\right) \middle| l,m,i \right\rangle \left\langle l,m,i \middle| \psi\left(\vec{k}\right) \right\rangle \quad (1)$$

where n, $\vec{k}$ denote band index and crystal momentum, respectively.

Data availability

All relevant data are available from the authors upon request.

ACKNOWLEDGEMENTS

The authors would like to acknowledge funding for this work by the Department of Energy (grant number: DE-FG02-03ER46066). This work utilized the Janus supercomputer, which is supported by the National Science Foundation (award number CNS-0821794) and the University of Colorado Boulder. The Janus supercomputer is a joint effort of the University of Colorado Boulder, the University of Colorado Denver and the National Center for Atmospheric Research. T.J. Nummy would like to acknowledge the NSF GRFP for their support. Department of Energy, grant number: DE-FG02-03ER46066. National Science Foundation, award number: CNS-0821794 (JANUS Supercomputer). National Science Foundation Graduate Research Fellowship Program.

AUTHOR CONTRIBUTIONS

T.J. Nummy performed the ARPES measurements, density functional calculations, data analysis, wrote and edited the manuscript. J.A.W. and Q.L. performed the Density Functional calculations. J.A.W., S.P., H.L., X.Z., N.C.P. all performed ARPES measurements. F.F.T. and H.Y.Y. synthesized the single crystals and edited the manuscript. D.S. D. directed the research and assisted in writing and edited the manuscript.

ADDITIONAL INFORMATION

Supplementary information accompanies the paper on the *npj Quantum Materials* website (https://doi.org/10.1038/s41535-018-0094-3).

Competing interests: The authors declare no competing interests.

Publisher's note: Springer Nature remains neutral with regard to jurisdictional claims in published maps and institutional affiliations.

REFERENCES

1. Tafti, F. F., Gibson, Q. D., Kushwaha, S. K., Haldolaarachchige, N. & Cava, R. J. Resistivity plateau and extreme magnetoresistance in LaSb. *Nat. Phys.* **12**, 272–277 (2015).
2. Zeng, M. et al. Topological semimetals and topological insulators in rare earth monopnictides. *Arxiv* 1504.03492. (2015).
3. Alidoust, N. et al. A new form of (unexpected) Dirac fermions in the strongly-correlated cerium monopnictides. *arXiv* 1604.08571. (2016).
4. Zeng, L. K. et al. Compensated semimetal LaSb with unsaturated magnetoresistance. *Phys. Rev. Lett.* **117**, 127204 (2016).
5. Ghimire, N. J., Botana, A. S., Phelan, D., Zheng, H. & Mitchell, J. F. Magnetotransport of single crystalline YSb. *J. Phys. Condens. Matter* **28**, 235601 (2016).
6. Wu, Y. et al. Unusual electronic properties of LaBi—a new topological semimetal candidate. *Phys. Rev. B* **94**, 081108 (2016).
7. Rodriguez-Martinez, L. & Attfield, J. Cation disorder and size effects in magnetoresistive manganese oxide perovskites. *Phys. Rev. B* **54**, R15622 (1996).
8. Protière, S., Couder, Y., Fort, E. & Boudaoud, A. The self-organization of capillary wave sources. *J. Phys. Condens. Matter* **17**, 45 S3529 (2005).
9. Rao, C. N. R. & Cheetham, aK. Giant magnetoresistance in transition metal oxides. *Science* **272**, 369–370 (1996).
10. Lenz, J. E. A Review of Magnetic Sensors. *Proc. IEEE* **78**, 973–989 (1990).
11. Wolf, A. S. A. et al. Spintronics: a spin-based electronics vision for the future. *Science* **294**, 1488–1495 (2001).
12. Tafti, F. F. et al. Temperature-field phase diagram of extreme magnetoresistance in lanthanum monopnictides. *Proc. Natl. Acad. Sci.* **12**, 272–277 (2016).
13. Liang, T. et al. Ultrahigh mobility and giant magnetoresistance in the Dirac semimetal Cd_3As_2. *Nat. Mater.* **14**, 280–284 (2015).
14. Xiong, J. et al. Anomalous conductivity tensor in the Dirac semimetal Na_3Bi. *Europhys. Lett.* **114**, 27002 (2015).
15. Shekhar, C. et al. Extremely large magnetoresistance and ultrahigh mobility in the topological Weyl semimetal candidate NbP. *Nat. Phys.* **11**, 645–649 (2015).
16. Huang, X. et al. Observation of the chiral-anomaly-induced negative magnetoresistance: In 3D Weyl semimetal TaAs. *Phys. Rev. X* **5**, 031023 (2015).
17. Ghimire, N. J. et al. Magnetotransport of single crystalline NbAs. *J. Phys. Condens. Matter* **27**, 152201 (2015).
18. Mun, E. et al. Magnetic field effects on transport properties of PtSn_4. *Phys. Rev. B* **85**, 035135 (2012).
19. Wang, K., Graf, D., Li, L., Wang, L. & Petrovic, C. Anisotropic giant magnetoresistance in $NbSb_2$. *Sci. Rep.* **4**, 7328 (2014).
20. Zhu, Z. et al. Quantum oscillations, thermoelectric coefficients, and the fermi surface of semimetallic WTe_2. *Phys. Rev. Lett.* **114**, 176601 (2015).
21. Niu, X. H. et al. Presence of exotic electronic surface states in LaBi and LaSb. *Phys. Rev. B* **94**, 165163 (2016).
22. Nayak, J. et al. Multiple Dirac cones at the surface of the topological metal LaBi. *Nat. Commun.* **8**, 13942 (2017).
23. Fu, L. & Kane, C. L. Topological insulators with inversion symmetry. *Phys. Rev. B* **76**, 045302 (2007).
24. Teo, J. C. Y., Fu, L. & Kane, C. L. Surface states and topological invariants in three-dimensional topological insulators: Application to Bi_{1-x} Sb_x. *Phys. Rev. B* **78**, 045426 (2008).
25. Cao, Y. et al. Mapping the orbital wavefunction of the surface states in three-dimensional topological insulators. *Nat. Phys.* **9**, 499–504 (2013).
26. Zhu, Z. H. et al. Layer-by-layer entangled spin-orbital texture of the topological surface state in Bi_2Se_3. *Phys. Rev. Lett.* **110**, 216401 (2013).
27. Guo, P. J., Yang, H. C., Zhang, B. J., Liu, K. & Lu, Z. Y. Charge compensation in extremely large magnetoresistance materials LaSb and LaBi revealed by first-principles calculations. *Phys. Rev. B* **93**, 235142 (2016).